DispatchDate: 29.06.2019 · ProofNo: 87, p.1

nature metabolism

LETTERS

https://doi.org/10.1038/s42255-019-0087-y

Role and therapeutic potential of dietary ketone bodies in lymph vessel growth

Melissa García-Caballero[1,2,10], Annalisa Zecchin[1,2,8,10], Joris Souffreau[1,2], Anh-Co Khanh Truong[1,2], Laure-Anne Teuwen[1,2], Wesley Vermaelen[3,4], Rosa Martín-Pérez[5,6,8], Pauline de Zeeuw[1,2], Ann Bouché[1,2], Stefan Vinckier[1,2], Ivo Cornelissen[1,2,9], Guy Eelen[1,2], Bart Ghesquière[3,4], Massimiliano Mazzone[5,6], Mieke Dewerchin[1,2] and Peter Carmeliet[1,2,7*]

Lymphatic vessels (LVs), lined by lymphatic endothelial cells (LECs), are indispensable for life[1]. However, the role of metabolism in LECs has been incompletely elucidated. In the present study, it is reported that LEC-specific loss of OXCT1, a key enzyme of ketone body oxidation[2], reduces LEC proliferation, migration and vessel sprouting in vitro and impairs lymphangiogenesis in development and disease in Prox1$^{\Delta OXCT1}\lambda$ mice. Mechanistically, OXCT1 silencing lowers acetyl-CoA levels, tricarboxylic acid cycle metabolite pools, and nucleotide precursor and deoxynucleotide triphosphate levels required for LEC proliferation. Ketone body supplementation to LECs induces the opposite effects. Notably, elevation of lymph ketone body levels by a high-fat, low-carbohydrate, ketogenic diet or by administration of the ketone body β-hydroxybutyrate increases lymphangiogenesis after corneal injury and myocardial infarction. Intriguingly, in a mouse model of microsurgical ablation of LVs in the tail, which repeats features of acquired lymphoedema in humans, the ketogenic diet improves LV function and growth, reduces infiltration of anti-lymphangiogenic immune cells and decreases oedema, suggesting a novel dietary therapeutic opportunity.

The lymphatic system is indispensable for life and its dysfunction contributes to various disorders[1]. In particular, insufficient LV formation or function results in lymphoedema, a chronic oedematous state of the skin involving swelling and fibroadipose tissue deposition in the extremities[3]. Lymphoedema is a common post-cancer treatment complication caused by lymphatic injury (surgical removal of lymph nodes)[4,5]. It is estimated that, among cancer patients, one in six who undergo treatment of breast cancer, melanoma, genitourinary or gynaecological tumours involving lymph node removal or radiotherapy will develop secondary lymphoedema[6,7]. Despite its medical importance, no approved pharmacological treatment is available, and only a symptom-controlling physiotherapy exists. Furthermore, although the importance of LECs in health and disease has been recognized, there are few reports on LEC metabolism[8,9].

It has recently been reported that LECs rely on fatty acid β-oxidation (FAO) for proliferation, migration and sprouting[8]. Furthermore, FAO facilitates LEC differentiation by generating acetyl-CoA for histone acetylation at lymphangiogenic genes, promoting their expression[8]. Notably, supplementation of acetate (which can be converted to acetyl-CoA) rescues the lymphangiogenesis defect caused by FAO inhibition, highlighting the importance of acetyl-CoA as a central hub in regulating LV growth[8]. Another source of acetyl-CoA is ketone bodies, energy-rich metabolites secreted by the liver[2]. In extrahepatic tissues, ketone bodies are oxidized in mitochondria into two molecules of acetyl-CoA (ketone body oxidation (KBO)) (Fig. 1a), which can then enter the tricarboxylic acid (TCA) cycle[2]. In the present study, the role of KBO in lymphangiogenesis was characterized.

It was first assessed whether LECs have access to β-hydroxybutyrate (β-OHB), the most abundant circulating ketone body in the blood[2]. In adult mice fed a chow diet, β-OHB was detectable in lymph (collected from the thoracic duct), at similar levels to those in plasma (blood collected from the vena cava) (Fig. 1b). To assess whether KBO is active in primary human dermal LECs (HDLECs), uniformly ^{13}C-labelled β-OHB ([U-^{13}C]β-OHB) was added as a supplement and the incorporation of ^{13}C-labelled carbons into acetyl-CoA was measured over time. [U-^{13}C]β-OHB was rapidly metabolized into acetyl-CoA, yielding an M+2 labelling of 12.5% after 24 h (Fig. 1c).

To determine the importance of KBO in HDLECs, the expression of 3-oxoacid-CoA-transferase-1 (OXCT1) (Fig. 1a), a rate-controlling enzyme of KBO[2], was silenced by transducing HDLECs with lentiviral vectors expressing two different, non-overlapping, specific shRNAs against *OXCT1*, which efficiently lowered its RNA and protein levels (see Supplementary Fig. 1a–c). OXCT1 knockdown (OXCT1^{KD}) diminished proliferation and migration of HDLECs (Fig. 1d,e), without affecting HDLEC survival (see Supplementary Fig. 1d–f). In addition, OXCT1^{KD} impaired sprouting of HDLEC spheroids, also when HDLECs were mitotically inactivated by mitomycin C (MitoC) to assess cell migration without the impact of proliferation (which contributes to sprouting) (Fig. 1f,g and

[1]Laboratory of Angiogenesis and Vascular Metabolism, VIB Center for Cancer Biology, Vlaams Instituut voor Biotechnologie, Leuven, Belgium. [2]Laboratory of Angiogenesis and Vascular Metabolism, Department of Oncology,Leuven Cancer Institute, Katholieke Universiteit Leuven, Leuven, Belgium. [3]Metabolomics Expertise Center, VIB Center for Cancer Biology, Vlaams Instituut voor Biotechnologie, Leuven, Belgium. [4]Metabolomics Expertise Center, Department of Oncology, Katholieke Universiteit Leuven, Leuven, Belgium. [5]Laboratory of Tumor Inflammation and Angiogenesis, VIB Center for Cancer Biology, Vlaams Instituut voor Biotechnologie, Leuven, Belgium. [6]Laboratory of Tumor Inflammation and Angiogenesis, Department of Oncology, Leuven Cancer Institute, Katholieke Universiteit Leuven, Leuven, Belgium. [7]State Key Laboratory of Ophthalmology, Zhongshan Ophthalmic Center, Sun Yat-Sen University, Guangzhou, China. [8]Present address: Janssen Immunosciences, World Without Disease Accelerator, Pharmaceutical Companies of Johnson and Johnson, Beerse, Belgium. [9]Present address: Department of Pharmacology, Research and Development, Janssen Pharmaceutical Company of Johnson and Johnson, Beerse, Belgium. [10]These authors contributed equally: M. García-Caballero, A. Zecchin. *e-mail: peter.carmeliet@kuleuven.vib.be

Uncorrected Proofs

see Supplementary Fig. 1g). Use of the second, non-overlapping shRNA (OXCT1^{KD2}) yielded similar results (see Supplementary Fig. 1h–k). Moreover, silencing of β-OHB dehydrogenase 1 (BDH1^{KD}) (see Supplementary Fig. 1l), the enzyme that metabolizes β-OHB to acetoacetate (Fig. 1a), impaired proliferation and migration as well as sprouting of HDLECs, phenocopying OXCT1^{KD} (Fig. 1h–k and see Supplementary Fig. 1m). Conversely, supplementation of ketone bodies (β-OHB, acetoacetate) to HDLECs promoted proliferation, migration and sprouting of HDLECs (see Supplementary Fig. 1n–r).

To explore whether OXCT1 controls lymphangiogenesis in vivo, *Oxct1*$^{lox/lox}$ mice[10] were intercrossed with an LEC-specific, tamoxifen-inducible, Cre driver line, that is *Prox1-Cre*^{ERT2} transgenic mice[11], to generate Cre-positive, LEC-specific, Oxct1-deficient mice (Prox1$^{\Delta OXCT1}$) or Cre-negative, control littermates (Prox1^{WT}) on tamoxifen treatment, yielding efficient and broad Oxct1 deletion in LECs (see Supplementary Fig. 2a–d). Embryonic lymphangiogenesis was defective in Prox1$^{\Delta OXCT1}$ embryos, as evidenced by the presence of oedema under the skin and impaired dermal LV growth at E15.5 (Fig. 1l–p). Using the corneal model of injury-induced lymphangiogenesis[12], it was observed that the LV area and branch point density were reduced in Prox1$^{\Delta OXCT1}$ mice (Fig. 2a–c), whereas CD31^{+} blood vessel growth was unaffected (see Supplementary Fig. 2e). Similar impairment of lymphangiogenesis was observed during the healing phase after myocardial infarction (Fig. 2d–f). Thus, LEC-specific loss of OXCT1 impaired developmental and pathological lymphangiogenesis.

Based on the above findings that KBO promotes lymphangiogenesis, it was explored whether supplementation of exogenous ketone bodies stimulates LV growth in vivo. Wild-type (WT) mice were fed a high-fat, low-carbohydrate, ketogenic diet (HFLC-KD), known to increase the levels of circulating ketone bodies[2], using chow diet as control. Mice fed an HFLC-KD had elevated β-OHB levels in plasma and lymph (see Supplementary Fig. 2f). An HFLC-KD caused slight variations in body weight and reduced glucose levels in plasma and lymph (see Supplementary Fig. 2g–i). As LECs also rely on glucose to sprout[9], it had been expected that the reduction in glucose availability would impair LV growth; however, an HFLC-KD stimulated LV growth in the cornea after thermal cauterization, as indicated by the increase in LV area and branch point density (Fig. 2g–i). The number of proliferating bromodeoxyuridine (BrdU)$^{+}$ LECs at the lymphatic front of the corneal LV network was increased on an HFLC-KD (Fig. 2j,k). To confirm that these effects were due to ketone bodies in the HFLC-KD, a β-OHB supplement was given to WT mice via daily intraperitoneal injections and a similar increase in lymphangiogenesis was observed (see Supplementary Fig. 2j–l). Comparable results were obtained in the myocardial infarction mouse model on feeding an HFLC-KD (Fig. 2l–n). Notably, an HFLC-KD or β-OHB supplementation failed to increase lymphangiogenesis in Prox1$^{\Delta OXCT1}$ mice, indicating that OXCT1-driven KBO was essential (Fig. 2o,p and see Supplementary Fig. 3a–h). Similar results were obtained when supplementing acetoacetate, the substrate for OXCT1 (see Supplementary Fig. 3i–j).

In line with the findings that ketone bodies are a source of acetyl-CoA (Fig. 1a), OXCT1^{KD} lowered the acetyl-Co:coenzyme A (CoA) ratio in HDLECs (Fig. 3a and see Supplementary Table 1) and the levels of TCA cycle intermediates (Fig. 3b and see Supplementary Table 1). It was reported that fatty acid-derived acetyl-CoA, together with an anaplerotic substrate, sustains the TCA cycle for deoxynucleotide triphosphate (dNTP) synthesis during proliferation of endothelial cells[8,13]. Similarly, in HDLECs, OXCT1^{KD} lowered the cellular pool of dNTPs (Fig. 3c and see Supplementary Table 1), paralleling the proliferation defect, and lowered the pool of the nucleotide precursors aspartate and glutamate, as well as the levels of ATP, CTP, GTP and UTP (Fig. 3d and see Supplementary Table 1). Similar effects were obtained using OXCT1^{KD2} (see Supplementary Fig. 4a–c and Supplementary Table 2). Conversely, ketone body supplementation to HDLECs caused the opposite effects, although these effects were modest, probably because these metabolites were already at near-maximal/optimal levels (Fig. 3e–g and see Supplementary Table 3). Thus, by sustaining the TCA cycle (presumably in conjunction with an anaplerotic substrate), KBO contributes to dNTP synthesis for DNA replication of HDLECs.

As the reducing equivalents generated during the conversion of β-OHB to acetyl-CoA can be delivered to the electron transport chain for ATP production, the oxygen consumption rate (OCR) was measured in HDLECs. OXCT1^{KD}, OXCT1^{KD2} or BDH1^{KD} modestly (but notably) reduced oxygen consumption linked to ATP synthesis (OCR$_{ATP}$) (Fig. 3h,i and see Supplementary Fig. 4d). Thus, HDLECs can utilize ketone bodies as an alternative energy source, even when glucose is available.

To further characterize the use of β-OHB in HDLECs, HDLECs were supplemented with [U-^{13}C]β-OHB. Isotopomer analysis revealed the incorporation of the ^{13}C label from [U-^{13}C]β-OHB into

Fig. 1 | KBO regulates lymphangiogenesis. a, Scheme of the KBO pathway (metabolic enzymes are indicated in green: BDH1; OXCT1; mThiolase; citrate synthase); the rate-controlling enzyme OXCT1 is boxed. **b**, LC-MS measurements of β-OHB levels in mouse plasma and lymph (expressed relative to plasma levels); plasma and lymph were collected from the vena cava and the thoracic duct, respectively ($n=4$ mice for each condition). **c**, Kinetic analysis of M+2 labelling from [U-^{13}C]β-OHB in acetyl-CoA in HDLECs ($n=4$ biologically independent samples used in independent experiments). **d**, [^{3}H]Thymidine incorporation into DNA in control and OXCT1^{KD} HDLECs ($n=5$ biologically independent samples used in independent experiments). **e**, Scratch wound migration assay using control and OXCT1^{KD} HDLECs ($n=5$ biologically independent samples used in independent experiments). **f**,**g**, Representative phase contrast images of control and OXCT1^{KD} HDLEC spheroids with and without MitoC treatment (**f**) and quantification of total sprout length (**g**) ($n=4$ biologically independent samples used in independent experiments). Scale bars, 100 µm. **h**, [^{3}H]Thymidine incorporation into DNA in control and BDH1^{KD} HDLECs ($n=5$ biologically independent samples used in independent experiments). **i**, Scratch wound migration assay using control and BDH1^{KD} HDLECs ($n=5$ biologically independent samples used in independent experiments). **j**,**k**, Representative phase contrast images of control and BDH1^{KD} HDLEC spheroids with and without MitoC treatment (**j**) and quantification of total sprout length (**k**) ($n=4$ biologically independent samples used in independent experiments). Scale bars, 100 µm. **l**, Stereomicrographs of wild-type (Prox1^{WT}) and mutant (Prox1$^{\Delta OXCT1}$) embryos at E15.5. Asterisks indicate subdermal oedema. Representative for $n=14$ Prox1^{WT} embryos and $n=10$ Prox1$^{\Delta OXCT1}$ embryos from three independent experiments (three litters). **m**, Representative images of the VEGFR-3^{+} dermal lymphatic network in E15.5 embryo back skins. White dashed lines delineate the midline gap between LV fronts. Insets to the right are magnifications of the respective boxed areas. Note the abnormal, enlarged LVs in Prox1$^{\Delta OXCT1}$ embryos. Scale bars, 500 µm. **n**–**p**, Quantifications of the midline gap size determined by LV outgrowth (**n**), LV branch point density (expressed as number of branch points mm^{-2}) (**o**) and LV length (expressed in µm) (**p**) per total area analysed ($n=14$ Prox1^{WT} mice; $n=10$ Prox1$^{\Delta OXCT1}$ mice, from three litters). For experiments involving embryos, 50 mg kg^{-1} of tamoxifen was administered to the pregnant dams daily by oral gavage between E8.5 and E10.5 of the pregnancy stage. Data are mean ± s.e.m. with individual data points shown. *$P<0.05$, NS, not significant, by two-tailed, one-sample, Student's *t*-test (**b**) or two-tailed, Student's *t*-test (**d**,**e**, **g**–**i**, **k**, **n**–**p**). Exact *P* values are as follows: **b**, 0.4220; **d**, 0.0399; **e**, 0.0019; **g**, control versus OXCT1^{KD}: 0.0094; control versus OXCT1^{KD} (+MitoC): <0.0001; **h**, 0.0130; **i**, 0.0169; **k**, control versus BDH1^{KD}: 0.0038; control versus BDH1^{KD} (+MitoC): <0.0001; **n**, 0.0465; **o**, 0.0199; **p**, 0.0216. Ctrl, control; DPM, disintegrations min^{-1}.

acetyl-CoA and TCA intermediates (Fig. 3j,k, control bars). When HDLECs were exposed to [U-^{13}C]β-OHB for 30 h to reach steady state, 12.5% of the ^{13}C label from [U-^{13}C]β-OHB was incorporated into acetyl-CoA M+2 in control HDLECs, which was reduced on OXCT1^{KD} (Fig. 3j and see Supplementary Fig. 4e for OXCT1^{KD2}). How a 12% incorporation of ^{13}C label from [U-^{13}C]β-OHB into acetyl-CoA suffices to induce the observed metabolic and biological phenotypes, and whether this relates to metabolic pathway compartmentalization, remain to be determined. In accordance, ^{13}C labelling from [U-^{13}C]β-OHB into the downstream TCA cycle intermediates citrate, aconitate, α-ketoglutarate (αKG), succinate, fumarate and malate was also decreased on OXCT1^{KD} in HDLECs (Fig. 3k and

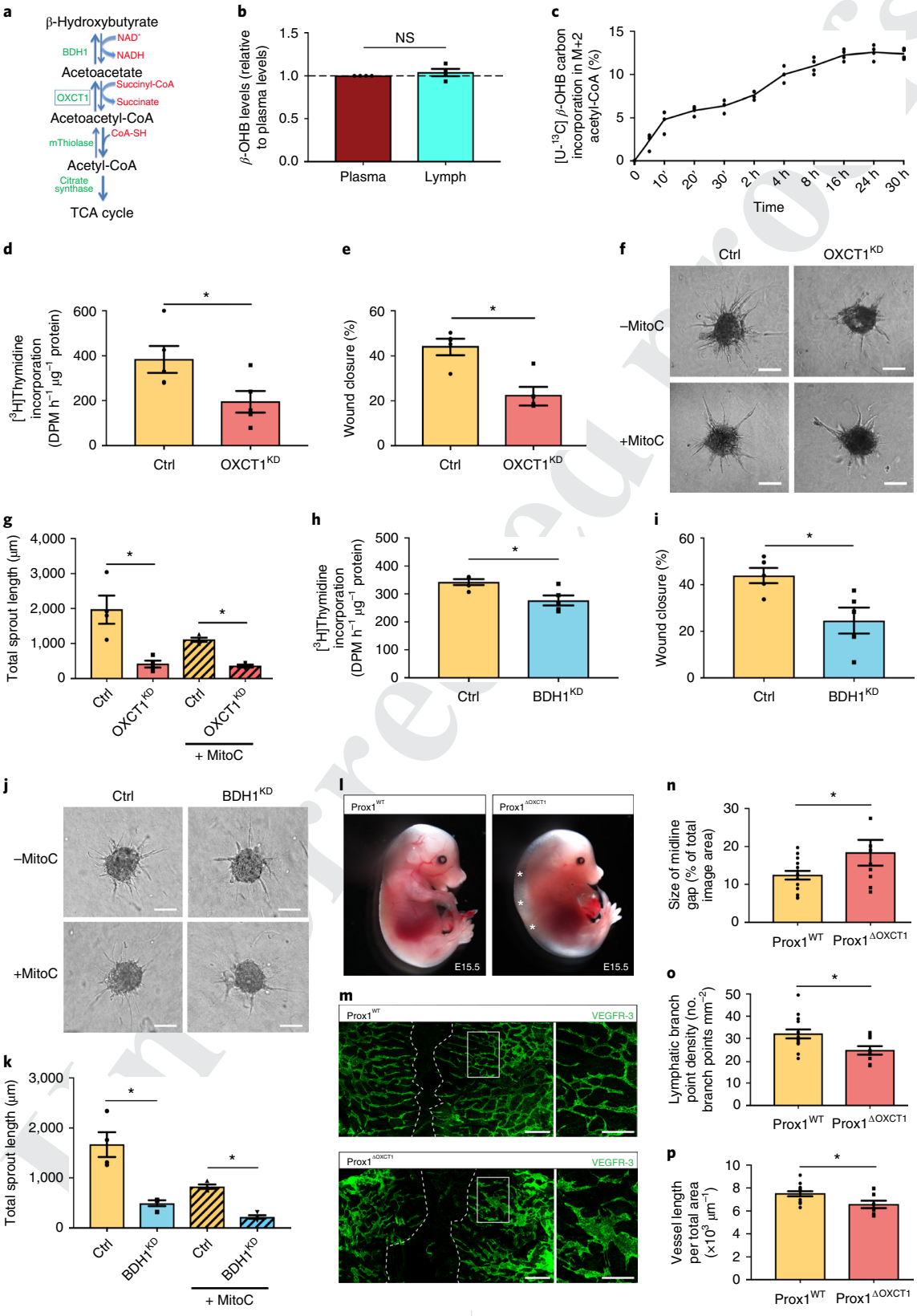

see Supplementary Fig. 4f for OXCT1^{KD2}). Thus, HDLECs metabolize β-OHB to acetyl-CoA and TCA cycle intermediates.

It was also explored whether ketone bodies could stimulate lymphangiogenesis, not only by sustaining the TCA cycle (together with other anaplerotic substrates), but also via additional mechanisms. First, ketone bodies are known to have contextual anti-inflammatory effects by directly affecting leukocytes[14–16]. In agreement, CD4$^+$ and CD8$^+$ T cell infiltration in lymphoedematous mouse tails (see below) was reduced on an HFLC-KD (Fig. 4a,b). Second, it was noticed that OXCT1^{KD} in HDLECs reduced the expression of lymphangiogenic genes (*PROX1*, *VEGFR-3*, *VEGF-C*, *TIE2*, *ANG1*) (see Supplementary Fig. 5a–e), although ketone body supplementation elevated expression levels of these genes at the messenger RNA (mRNA) and protein level (see Supplementary Fig. 5f–k).

This raised the question of whether ketone bodies are involved in the epigenetic regulation of lymphangiogenic gene expression, a plausible mechanism given that LECs utilize FAO-derived acetyl-CoA to fuel histone acetylation and regulate lymphatic gene expression during LEC differentiation[8], and that ketone bodies can inhibit histone deacetylases[2]. However, OXCT1^{KD} did not alter acetylation of histones H2, H3 and H4 (see Supplementary Fig. 5l—left panel), and of H4K^{8}ac (see Supplementary Fig. 5l—top right panel). In addition, neither OXCT1^{KD} nor HFLC-KD altered acetylation of histone H3 at Lys^9 (H3K^{9}ac), a marker of active gene promoters that is sensitive to acetyl-CoA levels[17,18] (see Supplementary Fig. 5l—bottom right panel, **m**). Thus, ketone bodies did not seem to directly control histone acetylation.

However, alternative epigenetic mechanisms were also considered, because reduced αKG levels and a lower αKG:succinate ratio on OXCT1^{KD} (see Supplementary Fig. 5n,o) could suppress transcription by increasing the trimethylation levels of H3K^{27} (H3K^{27}me$_3$)[19–22]. Indeed, OXCT1^{KD} in HDLECs modestly increased the H3K^{27}me$_3$ levels (see Supplementary Fig. 5p), whereas trimethylation of H3K^{36} and H3K^{79} also tended to increase but without reaching statistical significance (not shown). A possible epigenetic effect of ketone bodies requires further study. Third, given the conversion of NAD$^+$ to NADH during ketolysis, it was also considered to be a possible effect of OXCT1^{KD} on redox homeostasis, but it was not possible to document any change (see Supplementary Fig. 5q–t).

It was then explored whether the use of an HFLC-KD, as a dietary approach, could improve lymphoedema. A preclinical mouse tail lymphoedema model was used that copies features of secondary lymphoedema in humans[23,24]. Notably, in mice fed an HFLC-KD, initiated 2 d after surgical removal of the dermal superficial and deep LVs in the tail, tail swelling was less pronounced (Fig. 4c), with tail volumes being ±50% lower at 2 and 3 weeks after surgery (Fig. 4d–f). An HFLC-KD also reduced dermal thickening (Fig. 4g,h), decreased LV dilatation (a hallmark of LV dysfunction[25]) and increased the number of LVs (Fig. 4i–k). In addition, lymphangiography after intradermal injection of Evans Blue dye revealed higher levels of Evans Blue in the iliac lymph nodes, the lymph and the plasma of mice fed an HFLC-KD compared with mice fed a chow diet (Fig. 4l–n), implying that an HFLC-KD stimulated the formation of new functional LVs across the wound that could drain interstitial fluid (and Evans Blue) from the oedematous tails. Possibly, the improved drainage and decreased oedema could also contribute indirectly to the reduced T cell accumulation mentioned above. Immunoblotting of lymphoedematous tail extracts showed increased protein levels of lymphangiogenic VEGFR-3, Tie2 and Ang1 on an HFLC-KD (see Supplementary Fig. 6).

In summary, it was demonstrated that ketone bodies stimulate LV growth and function, partly by generating acetyl-CoA to sustain the TCA cycle (probably together with an anaplerotic substrate) for nucleotide synthesis during LEC replication, and by generating reducing equivalents to sustain mitochondrial respiration and ATP production. Although not obviously regulating redox homeostasis, ketone bodies may stimulate lymphangiogenesis via additional effects, such as by suppressing the accumulation of anti-lymphangiogenic inflammatory immune cells or by stimulating lymphangiogenic gene expression (although a possible epigenetic mechanism requires additional evidence).

Exogenous supplementation of β-OHB, via a ketogenic diet or intraperitoneal injections, stimulates lymphangiogenesis in vivo and ameliorates lymphatic dysfunction and lymphoedema. This is noteworthy, given that current treatment of lymphoedema is largely symptomatic (including compression garments to reduce swelling, and so on), offering only stabilization and prevention of exacerbation of symptoms, but not providing a cure. A small-size study reported that a ketogenic diet reduced limb volume and

Fig. 2 | KBO promotes lymphangiogenesis in vivo. a–c, Representative images of LYVE1$^+$ LV (green) and CD31$^+$ blood vessel (red) outgrowth in cauterized corneas of Prox1^{WT} and Prox1$^{\Delta OXCT1}$ mice (**a**), quantification of LV area (**b**) and LV branch point density (**c**) ($n=13$ Prox1^{WT} mice; $n=14$ Prox1$^{\Delta OXCT1}$ mice). Scale bars, 500 µm. **d–f**, Representative images of LYVE1$^+$ LVs (green) in infarcted myocardium of Prox1^{WT} and Prox1$^{\Delta OXCT1}$ mice (**d**), quantification of LV area (**e**) and LV branch point density (**f**) ($n=9$ mice for each condition). The white line denotes the circumference of the whole heart. Scale bars, 2.5 mm. **g–i**, Representative images of LYVE1$^+$ LV (green) and CD31$^+$ blood vessel (red) outgrowth in cauterized corneas of WT mice receiving a chow diet or HFLC-KD (**g**), and quantification of LV area (**h**) and LV branch point density (**i**) ($n=12$ mice for each condition). Scale bars, 500 µm. **j,k**, Representative images of BrdU$^+$ (red) LYVE1$^+$ (green) LECs in cauterized corneas (**j**) and density of BrdU$^+$ LECs (**k**) in WT mice receiving a chow diet or HFLC-KD ($n=11$ mice for each condition); confocal images were carefully inspected at different *Z*-planes to verify that the BrdU$^+$ cells were LYVE1$^+$ LECs. Scale bars, 500 µm. Insets in **j** are magnifications of the respective boxed areas; arrowheads denote BrdU$^+$ LECs. Scale bars, 250 µm. **l–n**, Representative images of LYVE1$^+$ LVs (green) in infarcted myocardium of WT mice receiving a chow diet or HFLC-KD (**l**), and quantification of LV area (**m**) and LV branch point density (**n**) ($n=9$ mice for each condition). The white line denotes the circumference of the whole heart. Scale bars, 2.5 mm. **o,p**, Quantification of corneal (**o**) or myocardial (**p**) LV area in Prox1^{WT} and Prox1$^{\Delta OXCT1}$ mice fed a chow diet or HFLC-KD on corneal (**o**) or myocardial (**p**) injury. In **o**, $n=13$ mice for Prox1^{WT} chow; $n=15$ mice for Prox1^{WT} HFLC-KD; $n=15$ mice for Prox1$^{\Delta OXCT1}$ chow; and $n=14$ mice for Prox1$^{\Delta OXCT1}$ HFLC-KD. In **p**, $n=9$ mice for all the groups. Mice were fed a chow diet or HFLC-KD for 9 d in the corneal injury model and for 20 d in the myocardial infarction model, initiated the day after the injuries and maintained until the day of sacrifice. Even though the mice used in **a–f**, **o** and **p** had a different genetic background (C57BL/6N), and values of the LV area and branch point density were higher than in the mice used in **g–n** (C57BL/6J), qualitatively similar data were obtained. The LV branch point density in **c**, **f**, **i** and **n** is expressed as number of branch points per mm^2. Note: tamoxifen (50 mg kg^{-1}) was administered for 5 consecutive days to 7- to 8-week-old Prox1^{WT} and Prox1$^{\Delta OXCT1}$ mice by oral gavage and experiments were started 1 week later. Data are mean ± s.e.m. with individual data points shown. *$P<0.05$, NS, not statistically significant, by two-tailed, Student's *t*-test (**b**, **c**, **e**, **f**, **h**, **i**, **k**, **m**, **n**) or multiple comparison tests of the one-way analysis of variance (**o**, **p**). Exact *P* values are as follows: **b**, 0.0341; **c**, 0.0448; **e**, 0.0035; **f**, 0.0056; **h**, 0.0114; **i**, 0.0375; **k**, 0.0308; **m**, 0.0375; **n**, 0.0480; **o**, Prox1^{WT} chow versus Prox1^{WT} HFLC-KD: 0.0389; Prox1^{WT} chow versus Prox1$^{\Delta OXCT1}$ chow: 0.0354; Prox1$^{\Delta OXCT1}$ chow versus Prox1$^{\Delta OXCT1}$ HFLC-KD: 0.9996; **p**, Prox1^{WT} chow versus Prox1^{WT} HFLC-KD: 0.0002; Prox1^{WT} chow versus Prox1$^{\Delta OXCT1}$chow: 0.0282; Prox1$^{\Delta OXCT1}$ chow versus Prox1$^{\Delta OXCT1}$ HFLC-KD: 0.7408.

improved quality of life in obese patients with limb lymphoedema, and ascribed these beneficial effects to weight loss[26]. The present study now reports a molecular explanation for the beneficial effect of ketone bodies. Altogether, the findings may raise interest in use of dietary metabolite supplements for treating secondary lymphoedema in patients.

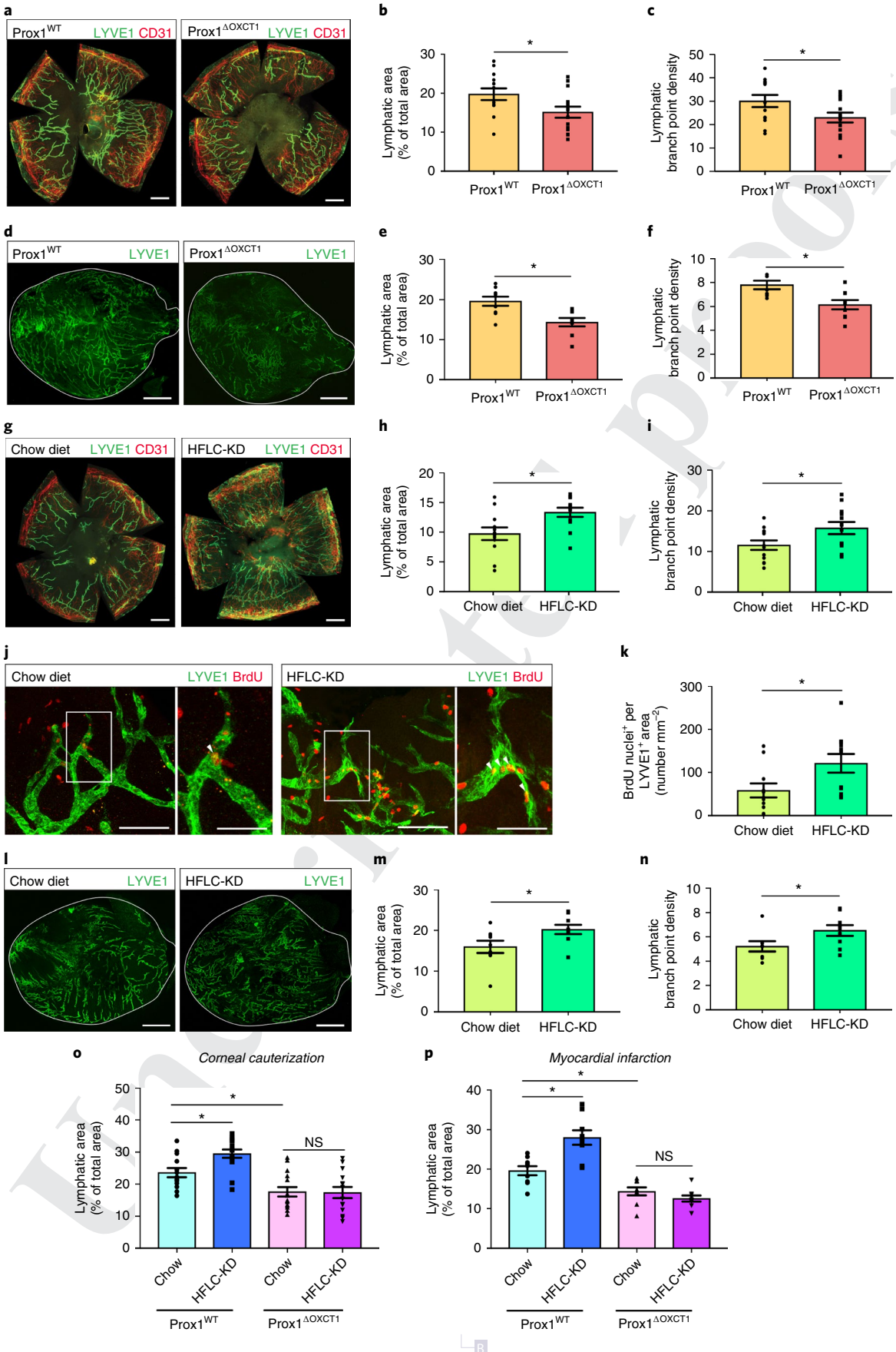

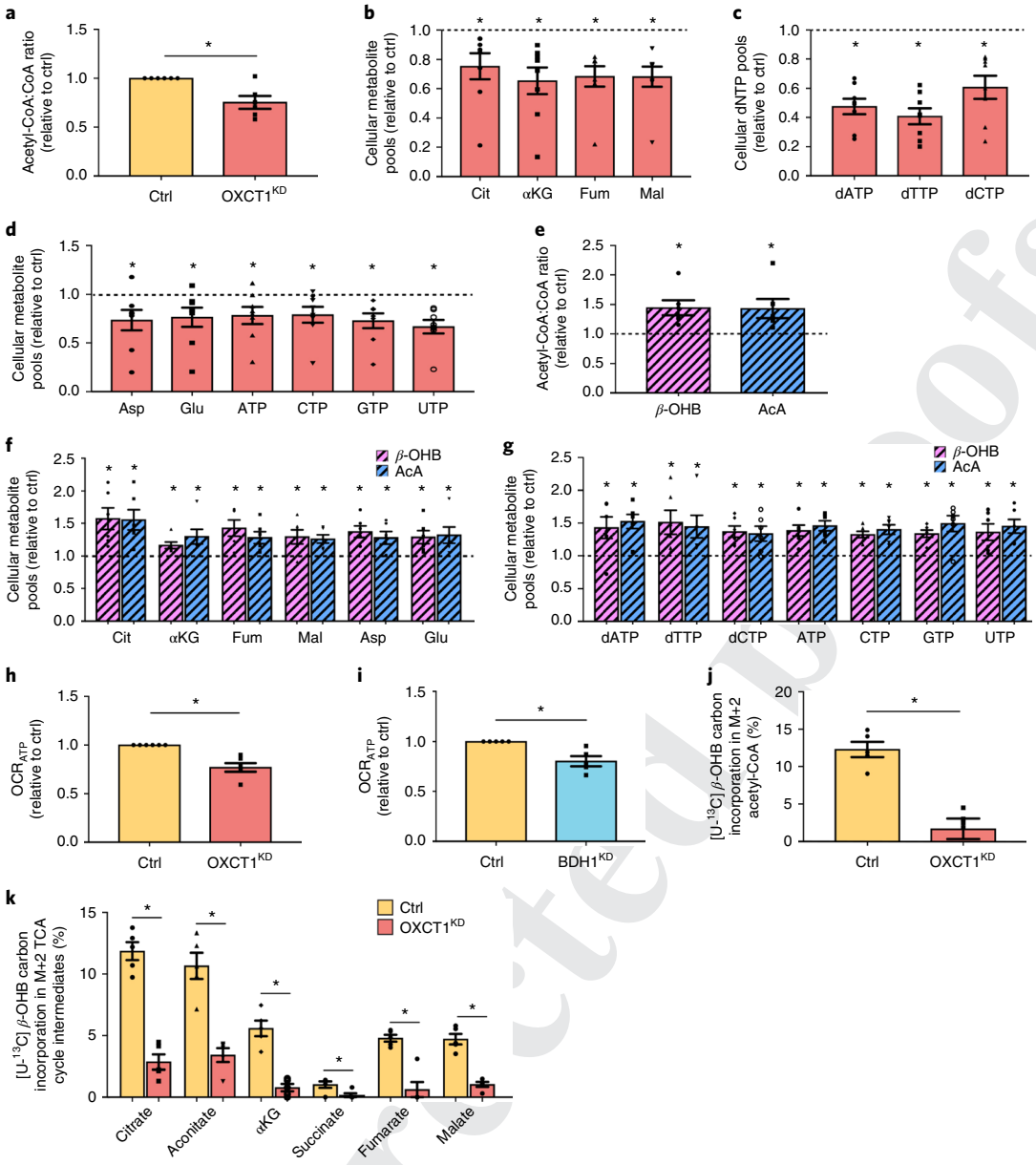

Fig. 3 | KBO contributes to sustaining the TCA cycle and to dNTP synthesis. a, Acetyl-CoA:CoA ratio in OXCT1^{KD} HDLECs, expressed relative to control HDLECs ($n=6$ biologically independent samples used in independent experiments). **b**, Cellular metabolite pool size normalized for protein content in OXCT1^{KD} HDLECs, expressed relative to control HDLECs ($n=8$ biologically independent samples used in independent experiments). **c**, Cellular dNTP pool size normalized for protein content in OXCT1^{KD} HDLECs, expressed relative to control HDLECs ($n=8$ biologically independent samples used in independent experiments). **d**, Cellular metabolite pool size normalized for protein content in OXCT1^{KD} HDLECs, expressed relative to control HDLECs ($n=8$ biologically independent samples used in independent experiments). **e**–**g**, Acetyl-CoA:CoA ratio (**e**), and cellular pool size, normalized for protein content, of TCA cycle metabolites, aspartate and glutamate (**f**), and nucleotides (**g**) in HDLECs incubated in medium supplemented with β-OHB (16 mM) or acetoacetate (4 mM), expressed relative to HDLECs in the control medium ($n=6$ biologically independent samples used in independent experiments). **h**,**i**, Quantification of OCR_{ATP} in OXCT1^{KD} HDLECs (**h**) and BDH1^{KD} HDLECs (**i**), relative to control HDLECs ($n=5$ biologically independent samples used in independent experiments). **j**, Analysis of M+2 labelling from [U-^{13}C]β-OHB into acetyl-CoA in control and OXCT1^{KD} HDLECs ($n=5$ biologically independent samples used in independent experiments). **k**, Analysis of M+2 labelling from [U-^{13}C]β-OHB into TCA cycle metabolites in control and OXCT1^{KD} HDLECs ($n=5$ biologically independent samples used in independent experiments). Data are mean ± s.e.m. with individual data points shown. *$P<0.05$ by two-tailed, one-sample, Student's t-test (**a**–**i**) or two-tailed, Student's t-test (**j**,**k**). Exact P values are as follows: **a**, 0.0125; **b**, control versus OXCT1^{KD}: 0.0265 (Cit); 0.0069 (αKG); 0.0028 (Fum); 0.0025 (Mal); **c**, control versus OXCT1^{KD}: <0.0001 (dATP); <0.0001 (dTTP); 0.0017 (dCTP); **d**, control versus OXCT1^{KD}: 0.0391 (Asp); 0.0491 (Glu); 0.0429 (ATP); 0.0373 (CTP); 0.0093 (GTP); 0.0020 (UTP); **e**, control versus supplemented HDLECs: 0.0177 (β-OHB); 0.0445 (acetoacetate); **f**, control versus supplemented HDLECs: 0.0188, 0.0163 (β-OHB, acetoacetate, respectively) (Cit); 0.0214, 0.0424 (β-OHB, acetoacetate, respectively) (αKG); 0.0196, 0.0267 (β-OHB, acetoacetate, respectively) (Fum); 0.0398, 0.0082 (β-OHB, acetoacetate, respectively) (Mal); 0.0086, 0.0319 (β-OHB, acetoacetate, respectively) (Asp); 0.0324, 0.0479 (β-OHB, acetoacetate, respectively) (Glu); **g**, control versus supplemented HDLECs: 0.0482, 0.0047 (β-OHB, acetoacetate, respectively) (dATP); 0.0387, 0.049 (β-OHB, acetoacetate, respectively) (dTTP); 0.076, 0.0310 (β-OHB, acetoacetate, respectively) (dCTP); 0.0057, 0.0019 (β-OHB, acetoacetate, respectively) (ATP); 0.0011, 0.0027 (β-OHB, acetoacetate, respectively) (CTP); 0.0017, 0.0099 (β-OHB, acetoacetate, respectively) (GTP); 0.0346, 0.0078 (UTP); **h**, 0.0033; **i**, 0.0178; **j**, 0.0002; **k**, <0.0001 (Cit); 0.0003 (aconitate); 0.0001 (αKG); 0.0229 (succinate); 0.0003 (Fum); <0.0001 (Mal). αKG, α-ketoglutarate; AcA, acetoacetate; Asp, aspartate; Cit, citrate; Ctrl/ctrl, control; Fum, fumarate; Glu, glutamate; Mal, malate.

Uncorrected Proofs

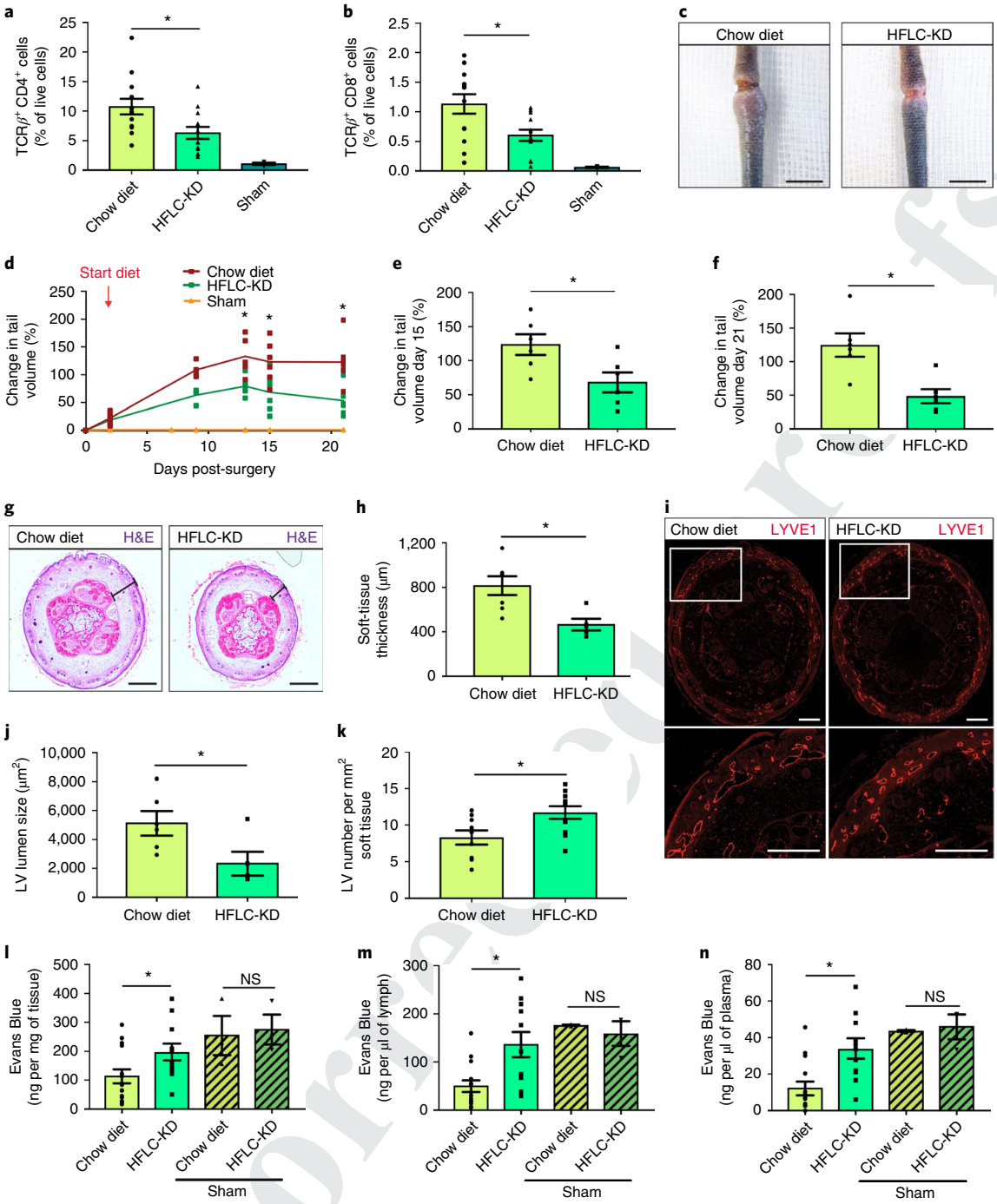

Fig. 4 | Effect of HFLC-KD supplementation on mouse tail lymphoedema. All panels show data obtained in WT mice subjected to surgical excision of tail superficial and deep collecting LVs or sham operation, receiving a chow diet or HFLC-KD. **a**,**b**, Quantification of TCRβ^+ CD4$^+$ cells (**a**) and TCRβ^+ CD8$^+$ cells (**b**) in the tail ($n=13$ mice for a chow diet and an HFLC-KD, $n=4$ mice for sham). **c**, Representative images of mouse tails at day 21 (D21). Scale bars, 1 cm. **d**, Percentage of tail volume changes versus day 0 (D0) post-surgery ($n=6$ independent experiments, with at least four mice per group in each experiment). **e**,**f**, Quantification of tail volume changes at day 15 (**e**) and day 21 (**f**) ($n=6$ independent experiments, with at least four mice per group in each experiment). **g**, Representative histological H&E images of tail tissue sections harvested 21 d after LV ablation. The black lines indicate soft-tissue thickness. Scale bars, 500 μm. **h**, Quantification of the soft-tissue thickness in mouse tails (D21) ($n=6$ independent experiments, with at least four mice per group in each experiment). **i**, Representative images of tail tissue sections harvested 21 d after LV ablation and immunostained for LYVE1 (red). Scale bars, 500 μm. Insets at the bottom in **i** are magnifications of the respective boxed area. **j**, LV lumen size quantification (D21) in mice fed a chow diet or an HFLC-KD ($n=6$ mice and $n=5$ mice for chow and HFLC-KD, respectively). **k**, LV number quantification per mm^2 of soft tissue (D21) in mice fed a chow diet or an HFLC-KD ($n=14$ mice for each condition). **l**–**n**, Quantification of Evans Blue accumulation in iliac lymph nodes (**l**), lymph (**m**) and plasma (**n**) ($n=16$ mice for chow diet, $n=12$ mice for an HFLC-KD, $n=3$ mice for sham groups); NS, not statistically significant. Mice were fed a chow diet or an HFLC-KD for 20 d, initiated 2 d after surgical intervention and until their sacrifice. Data are mean ± s.e.m. with individual data points shown. *$P<0.05$, NS, not statistically significant, by two-tailed, Student's *t*-test. Exact *P* values are as follows: **a**, 0.0134; **b**, 0.0098; **d**, 0.0351 (day 13); 0.0394 (day 15); 0.0037 (day 21); **e**, 0.0394; **f**, 0.0037; **h**, 0.0098; **j**, 0.0366; **k**, 0.0178; **l**, chow versus HFLC-KD: 0.0385; chow versus HFLC-KD (sham): 0.8995; **m**, chow versus HFLC-KD: 0.0030; chow versus HFLC-KD (sham): 0.5351; and **n**, chow versus HFLC-KD: 0.0019; chow versus HFLC-KD (sham): 0.7021.

Methods

Cell culture. HDLECs were isolated from foreskin biopsies (obtained with approval from the Medical Ethical Committee KU Leuven/UZ Leuven (file no. S57123) and informed consent from all subjects). After dispase digestion to remove the epidermis (12 h incubation at 4 °C with 2.5 U ml^{-1} of dispase II) (Sigma-Aldrich), collagenase digestion to harvest all the dermal cells (75 min incubation at 37 °C with 0.2% collagenase I solution; Thermo Fisher Scientific), including endothelial cells (ECs), was performed. Immunomagnetic beads (Miltenyi Biotec) were used to isolate CD45$^-$CD31$^+$ Podoplanin$^+$ cells (LECs), which were maintained in Endothelial Cell Growth Medium (EGM)-MV2 (Promocell)[27]. For the in vitro experimental procedures, '*n*' refers to the number of independent experiments performed on different days, with different, independent batches of HDLECs.

Lentiviral transductions. The shRNA oligonucleotides used to silence OXCT1 (TRCN0000036034: KD, used in most of the experiments; and TRCN0000036034: KD2; used for confirmatory experiments in Supplementary Figs. 2 and 4) and *BDH1* (TRCN0000028460) were cloned into the pLKO-shRNA vector (Sigma-Aldrich) and empty vectors were used as negative controls. Lentiviral particles were produced in 293 T cells and were used at a multiplicity of infection of 20 to transduce HDLECs. Cells were transduced overnight in the presence of 0.5 µg ml^{-1} of polybrene and re-fed with fresh medium the next day. Transduced cells were used in functional assays at least 3–4 d post-transduction.

RNA analysis. Total RNA from cell cultures was purified using the PureLink-RNA Mini Kit (Thermo Fisher Scientific) according to the manufacturer's instructions; quality and quantity were measured on a NanoDrop (Thermo Fisher Scientific). Complementary DNA (cDNA) synthesis was performed using the iScript-cDNA-synthesis kit (Bio-Rad). RNA expression analysis was performed using Taqman quantitative real-time PCR (qRT-PCR) using premade primer sets (Thermo Fisher Scientific and IDT; premade primer/probe set identification numbers are available on request). Expression levels were calculated as copies of mRNA per 1,000 copies of hypoxanthine–guanine phosphoribosyltransferase mRNA.

Proliferation assay. Cell proliferation was determined by incubating HDLECs with 1 µCi ml^{-1} of [^{3}H]thymidine (Perkin Elmer) for 24 h. Thereafter, cells were fixed with 100% ethanol for 15 min at 4 °C, precipitated with 10% trichloroacetic acid and lysed with 0.1 M NaOH. The amount of [^{3}H]thymidine incorporated into DNA was measured using scintillation counting[13].

Scratch wound migration assay. Scratch wounds were applied on confluent HDLEC monolayers using a 200-µl pipette tip and photographed at 0 and 16 h of incubation in the presence of 500 µg ml^{-1} of MitoC (Sigma-Aldrich). The migration distance (gap area) was measured using the National Institutes of Health (NIH) ImageJ software package and expressed as percentage wound closure (gap area at T0 minus gap area at T16 as a percentage of gap area at T0)[13].

Spheroid sprouting assay. HDLECs were incubated overnight in hanging drops in EGM-MV2 medium containing methylcellulose (20 vol% of a 1.2% solution of methylcellulose 4,000 cP) (Sigma-Aldrich) to form spheroids. Spheroids were then embedded in collagen gel and cultured in media supplemented with 100 ng ml^{-1} of recombinant human vascular endothelial growth factor (VEGF)-C (Peprotech) for 48 h[8]. Where indicated, the spheroid sprouting assay was performed with the addition of 500 µg ml^{-1} of MitoC to the medium on spheroids embedding in the collagen gel. Spheroids were fixed with 4% paraformaldehyde and phase contrast images were taken with the DMI6000B (Leica) microscope. Quantification of the total sprout length (cumulative length per spheroid) and number of sprouts per spheroid was done using the NIH ImageJ software package.

^{13}C tracer experiments. Cells were incubated in media containing [U-^{13}C]β-OHB (0.5 mM; Cambridge Isotope Laboratories, Inc.) for 24 h (steady state), or other indicated time points in the kinetic experiments (see Fig. 1c), and samples were processed to analyse tracer incorporation by liquid chromatography–mass spectrometry (LC-MS)[8].

Metabolite pool and isotopomer labelling analysis by LC-MS. Metabolites were extracted from 300,000 cells in 250 ml of a 50:30:20 (methanol:acetonitrile:10 mM Tris, pH 9.3) extraction buffer. Extraction samples were then centrifuged for 5 min at 20,000*g* and the supernatant was transferred to LC-MS vials. The cell pellet was lysed and used to measure protein levels for normalization purposes. Targeted measurements of acetyl-CoA, coenzyme A, citrate, aconitate, αKG, succinate, fumarate, malate, aspartate, glutamate, ribonucleotide triphosphates (rNTPs) and dNTPs, oxidized glutathione, reduced glutathione, NAD$^+$, NADH, NADP$^+$ and NADPH were performed using a Dionex UltiMate 3000 LC System (Thermo Fisher Scientific) equipped with a C-18 column (Acquity UPLC-HSST T3 1.8 µm; 2.1 × 150 mm, Waters) coupled to a Q Exactive Orbitrap mass spectrometer (Thermo Fisher Scientific) operated in negative ion mode. Among the dNTPs, dGTP analysis was not taken into account, because, due to co-elution of dGTP with ATP, the dGTP cannot purely be distinguished from ATP by mass. Practically, 5 µl of sample was injected on the Dionex UltiMate 3000 LC System and a step gradient was carried out using solvent A (10 mM tributylamine and 15 mM acetic acid) and solvent B (100% methanol). The gradient started with 0% solvent B and 100% solvent A and remained at 0% B until 2 min post-injection. A linear gradient to 37% B was carried out until 7 min and increased to 41% until 14 min. Between 14 min and 26 min the gradient increased to 100% B and remained at 100% B for 4 min. At 30 min the gradient returned to 0% B. The chromatography was stopped at 40 min. The flow was kept constant at 250 µl min^{-1} as the column was placed at 40 °C throughout the analysis. The MS operated in full scan–secondary ion mass (SIM) (negative mode) using a spray voltage of 3.2 kV, capillary temperature 320 °C, sheath gas at 10.0, auxiliary gas at 5.0. For full scan–secondary ion mass mode, an AGC target was set at 1e6 using a resolution of 70,000, with a maximum IT of 256 ms. Data collection was performed using Xcalibur software (Thermo Fisher Scientific).

Oxygen consumption rate. Cells were seeded at 40,000 cells per well on Seahorse XF24 tissue culture plates (Agilent) the day before the assay. The measurement of oxygen consumption was performed at 6-min intervals (2 min mixing, 2 min delay, 2 min measuring) using the Seahorse XF24 analyser. Inhibitors were used at the following concentrations: oligomycin (1.2 µM), antimycin (1 µM), carbonyl cyanide-4-(trifluoromethoxy)phenylhydrazone (5 µM). The data were normalized to protein content, determined by BCA assay (Thermo Fisher Scientific) on lysis of the cells (using radioimmunoprecipitation assay buffer) (see below) immediately after the assay[28].

LDH assay. Cell death was measured by determining the lactate dehydrogenase release in the medium using the Cytotoxicity Detection Kit (Roche Applied Science) according to the manufacturer's specifications, whereby low lactate dehydrogenase release signifies low cell death and high survival.

Apoptosis measurements. *Cleaved caspase-3 immunostaining*: HDLECs present in the medium and trypsinized adherent cells were pooled, then subjected to a centrifuge spin and resuspended in phosphate-buffered saline (PBS). From this suspension, aliquots were deposited on slides using a cytospin centrifuge, fixed and stained for cleaved caspase-3 (Cell Signaling) and actin (Alexa fluor 488 phalloidin; Thermo Fisher Scientific); nuclei were stained with Hoechst 33258 (1:1,000 in PBS)[28]. The percentage of apoptotic cells was determined by counting the cleaved caspase-3$^+$ cell fraction in at least six random microscopy fields per HDLEC donor. *Annexin V immunocytochemical staining*: HDLECs present in the medium and trypsinized adherent cells were pooled, pelleted and resuspended in binding buffer containing 10 mM 4-(2-hydroxyethyl)-1-piperazine-ethanesulfonic acid, 140 mM NaCl, 2.5 M $CaCl_2$, pH 7.4 at a density of 200,000 cells per 0.1 ml. Anti-annexin V antibody (5 µl per 0.1 ml; APC, Thermo Fisher Scientific) was then added at room temperature in the dark for 15 min. After washing, propidium iodide (10 µg ml^{-1} final concentration; Thermo Fisher Scientific) was added for 5 min before the FACS (BD FACSAria III) experiment. Analyses were performed using FlowJo software (FlowJo, LLC).

Ketone body supplementation in vitro. DL-β-OHB (16 mM; Sigma-Aldrich) and acetoacetate (4 mM; Sigma-Aldrich) were added to a customized medium containing 1 mM glucose and 0.6 mM glutamine. The optimal DL-β-OHB concentration was determined in pilot dose–response experiments; it cannot be formally excluded that this high concentration may also induce metabolism-independent signalling. As acetoacetate is a lithium salt, lithium chloride (Sigma-Aldrich) was included in the control conditions for the acetoacetate treatment.

Histone collection. HDLECs were collected and resuspended in cold nuclear isolation buffer (15 mM Tris-HCl,(pH 7.5, 60 mM KCl, 15 mM NaCl, 5 mM $MgCl_2$, 1 mM $CaCl_2$, 250 mM sucrose, freshly added: 1 mM dithiothreitol, 1× protease inhibitors (Roche), 10 mM sodium butyrate, 0.1% NP-40). The collected samples were incubated for 30 min on a rotator at 4 °C to promote hypotonic swelling of cells and lysis by mechanical shearing during rotation. Nuclei were pelleted at 21,000*g* for 5 min at 4 °C and immediately resuspended in 0.4 M H_2SO_4 followed by incubation overnight at 4 °C. After centrifugation at 21,000*g* for 10 min at 4 °C, histones were precipitated from the supernatant by addition of 20% trichloroacetic acid for 2 h, followed by centrifugation at 21,000*g* for 10 min at 4 °C. Pellets were washed twice with acetone. Histone proteins were resuspended in water and used for immunoblot analysis[8].

Bicinchoninic acid assay. Bicinchoninic acid assay (Thermo Fisher Scientific) was used to determine protein content. Cells were lysed using radioimmunoprecipitation assay buffer (20 mM Tris-HCl, pH 7.5 containing 150 mM NaCl, 1 mM disodium ethylenediaminetetraacetate and 1 mM ethylene glycol-bis(β-aminoethyl ether)-tetraacetic acid). The bicinchoninic acid assay was performed according to the manufacturer's guidelines.

Protein analyses. Lysates were separated by sodium dodecyl sulfate/polyacrylamide gel electrophoresis under reducing conditions, transferred to a poly(vinylidene difluoride) membrane and analysed by immunoblotting. Primary

antibodies used were against OXCT1 (Proteintech), pan-acetyl lysine (Active Motif), tubulin, glutaraldehyde 3-phosphate dehydrogenase, histone H3K^{9}ac, histone H4K^{8}ac, histone H3K^{27}me$_3$, histone H2, histone H3, histone H4 (Cell Signaling), VEGFR-3, Tie2 (Santa Cruz Biotechnology) and Ang1 (Thermo Fisher Scientific). Membranes were probed with the appropriate horse radish peroxidase-coupled secondary antibody and signal was detected using the ECL system (Amersham Biosciences) according to the manufacturer's instructions. Densitometric analyses were performed using NIH ImageJ software.

ROS analysis. Intracellular reactive oxygen species (ROS) levels were measured by FACS using the acetyl ester 5(and 6)-chloromethyl-20,70-dichlorodihydrofluorescein diacetate (CM-H_2DCFDA), according to the manufacturer's instructions (Thermo Fisher Scientific). The intracellular ROS levels were determined by pre-incubation of the HDLECs for 30 min with 10 mM CM-H_2DCFDA and the hydrogen-peroxide-scavenging capacity was determined after a subsequent incubation for 2 h with 100 mM H_2O_2 (Merck Millipore) in serum-free M199 medium (Thermo Fisher Scientific). Data were analysed using FlowJo software.

Mice. To obtain a tamoxifen-inducible, LEC-specific *Oxct1* knock-out line, *Oxct1*$^{lox/lox}$ mice[10] (provided by P. Crawford) were intercrossed with *Prox1-Cre*^{ERT2} mice[11] (provided by T. Mäkinen) generating *Prox1-Cre*^{ERT2};*Oxct1*$^{lox/lox}$ C57BL/6N mice. On subsequent intercrossing with double fluorescent mT/mG Cre reporter mice C57BL/6J[29], the resulting Prox1$^{\Delta OXCT1}$:mTmG mice allowed determination of recombination efficiency after tamoxifen treatment. Correct Cre-mediated excision of the floxed OXCT1 segment in tamoxifen-treated Prox1$^{\Delta OXCT1}$ mice was confirmed via PCR or qRT-PCR analysis of genomic DNA and RNA, respectively, using standard procedures. Tamoxifen (50 mg kg^{-1}) was administered for 5 consecutive days to 7- to 8-week-old female mice by oral gavage and experiments were started 1 week later. For experiments involving embryos, tamoxifen was administered to the pregnant dams daily (50 mg kg^{-1}) between E8.5 and E10.5. All experimental procedures were approved by the Institutional Animal Ethics Committee (file no. ECD 116/2014; Katholieke Universiteit Leuven, Belgium). In all the experimental procedures involving mice, littermate controls were used.

LEC isolations and RNA extraction. Murine LECs were isolated from liver, heart, lung and spleen of adult mice[30]. Briefly, mice were anaesthetized with ketamine/xylazine (intraperitoneal injection of 100 mg kg^{-1} body weight of ketamine (Eurovet Animal Health B.V.) and 10 mg kg^{-1} body weight of xylazine (VMD)) and the perfusion procedure was started once the withdrawal reflex was absent in pelvic limbs. Mice were perfused with 3 ml PBS followed by organ dissection, and dissociation in 3 ml of a Dulbecco's modified Eagle's medium-based digestion buffer containing 0.2% collagenase II and 0.2% collagenase IV (lungs, hearts), 0.1% collagenase I and 0.1% collagenase II (livers), 0.1% collagenase II and 0.25% collagenase IV (spleen) or dispase II (2.5 U ml^{-1}) (livers and hearts) (Thermo Fisher Scientific), and 250 mg ml^{-1} of DNase (Sigma-Aldrich), 2 mM $CaCl_2$, 1% antibiotic/antimycotic, at a perfusion rate of 1 ml min^{-1}. Lungs and hearts were further dissociated using the gentleMACS dissociator system (MACS Technology, Miltenyi Biotec). Next, samples were centrifuged, resuspended in 5 ml PBS-based wash buffer (containing 0.5% BSA and 2 mM ethylenediaminetetraacetic acid) and applied to a pre-separation 70-µm filter (Corning). The filtered cells were washed twice with wash buffer and ECs were selected using CD31 MicroBeads according to the manufacturer's instructions (MACS Technology, Miltenyi Biotec). Single-cell suspensions were stained with a viability dye (eBioscience eFluor 450, Thermo Fisher Scientific), CD45-PeCy7 (eBioscience, Thermo Fisher Scientific), podoplanin-APC (BioLegend), CD31-FITC (Thermo Fisher Scientific) at 4 °C for 30 min. Next, based on antibody staining, viable, CD45$^-$, CD31$^+$, podoplanin$^+$ LECs were FACS (BD FACSAria III) sorted, and RNA extracted using the RNeasy Micro Kit (QIAGEN) was converted to cDNA using the SuperScript III First Strand cDNA Synthesis Kit (Thermo Fisher Scientific). RNA expression analysis was performed by Taqman quantitative RT-PCR (Thermo Fisher Scientific).

Lymph and plasma collection. Blood and lymph were collected from the vena cava and the thoracic duct, respectively, in anaesthetized mice. Samples were then centrifuged at 800*g* for 10 min to remove the cellular components.

Analysis of embryonic development. At E.15.5, the pregnant dams were euthanized by cervical dislocation and the uteri removed. Blood flow/viability in embryos was assessed by counting the heart rate either through the yolk sac vessels or directly on the heart using a stereomicroscope. Embryos were dissected and the yolk sacs were washed with PBS and used for genotyping. Stereomicrographs to check the presence/absence of subdermal oedema were taken using a LUMAR V12 stereomicroscope (Zeiss).

Developmental lymphangiogenesis. Lymphangiogenesis was assessed by analysis of the anterior, dorsal, dermal LV network at E15.5[8]. Briefly, embryos were fixed in 1% paraformaldehyde for 10 min before the dorsal skin was dissected, and the epidermal and dermal layers were separated under a dissection microscope. Dissected back skins were permeabilized overnight (0.5% Triton X-100, 0.01% sodium deoxycholate, 1% BSA, 0.02% sodium azide), immunostained for VEGFR-3 (R&D Systems) and images were taken with the LSM780 (Zeiss) confocal microscope. Quantification of the midline gap size, branch point density (number of branch points per mm^2) and vessel length were performed using NIH ImageJ software.

Corneal cauterization assay. Corneal lymphangiogenesis was induced by thermal cauterization[8]. After anaesthetizing 8- to 12-week-old female mice with an intraperitoneal injection of ketamine (100 mg kg^{-1} body weight) and xylazine (10 mg kg^{-1} body weight), the local anaesthetic (Unicaine 0.4%; Théa Pharma) was applied to the eye and the central cornea was thermally cauterized using ophthalmic cautery (Optemp II V; Alcon Surgical). Mice were fed chow or an HFLC-KD (94.1% fat, 1.3% carbohydrates, 4.6% protein; Bio-Serv), or injected intraperitoneally with saline or β-OHB (200 mg kg^{-1}; Sigma-Aldrich) solutions for 9 d (initiated the day after induction of the corneal injury and maintained until sacrifice). For visualization of blood and lymph vessels, cauterized corneas were isolated and the whole mount immunostained for CD31 (BD Biosciences) and LYVE1 (Angiobio), respectively, flat mounted and imaged using the DMI6000B (Leica) microscope. Analyses of the lymphatic area (LYVE$^+$ area as a percentage of the total corneal area) and branch point density (number of branch points mm^{-2}) were performed. BrdU (Sigma-Aldrich) incorporation was assessed by injecting BrdU (150 mg kg^{-1}) in the tail vein 2 h before sacrifice. For detection of histone H3K^{9}ac in lymphatic vessels, cauterized corneas were immunohistochemically stained for VEGFR-3 (R&D Systems) and H3K^{9}ac (Cell Signaling). Quantification of the level of H3K^{9}ac fluorescence of LEC nuclei was done using NIH ImageJ software. Briefly, the Hoechst 33342$^+$ H3K9ac$^+$ nuclei within the lymphatic vessel (VEGFR-3$^+$ area) were individually circled, and the corrected total cell (nucleus) fluorescence (CTCF = integrated density − (area of selected nucleus × mean background fluorescence intensity)) was determined per image and expressed in arbitrary units.

Myocardial infarct model. An incision in the third left intercostal space was made in anaesthetized mice fixed in a supine position. Thereafter, muscles of the chest wall were prised apart, giving access to the coronary arteries, and a ligation was performed in the centre of the descending branch of the left coronary artery. The incision wound was closed and mice were left on a heated surgical table to recover. Mice were fed chow or an HFLC-KD or were injected intraperitoneally with either saline or β-OHB (200 mg kg^{-1}) for 20 d (initiated the day after induction of the infarcts and maintained until sacrifice). Whole-mount LYVE1 (Angiobio) immunostaining was performed on hearts and they were imaged using the LSM780 (Zeiss) confocal microscope. The LYVE$^+$ area was quantified using Leica MM AF morphometric analysis software (Leica Microsystems) and expressed as the percentage of the total heart area; branch point density was expressed as the number of branch points per mm^2.

Lymphoedema model. Acquired lymphoedema was surgically induced in the tails of 8- to 12-week-old C57BL/6J female mice through a circumferential skin excision made 20 mm distal to the base of the mouse tail, followed by ablation of the deep and superficial lymphatic vessels[23,24]. For sham controls, only the circumferential skin excision was performed. Mice were fed chow or an HFLC-KD, for 20 d (initiated 2 d after surgical removal and maintained until sacrifice). Tail pictures were captured at different time points and the oedema volume quantified according to the truncated cone formula ($V = 1/3(\pi \times h \times (R^2 + R \times r + r^2))$, V is the volume, and h is the height, R the bigger radius and r the smaller radius of the cone)[23,24]. H&E staining and LYVE1 (Angiobio) immunostainings were performed on histological tail sections. Soft-tissue thickness, vessel dilatation and number of LVs within the soft tissue were quantified using NIH ImageJ software. For the analysis of the immune cell infiltration, oedematous tail tissues were collected, the epidermis was removed by incubation with dispase (2.5 U ml^{-1} for 60 min at 37 °C) and the dermis was digested (0.1% collagenase II, 0.25% collagenase IV using the gentleMACS dissociator system), yielding single-cell suspensions that were incubated with a panel of different antibodies for the detection of specific inflammatory markers: viability dye eBioscience eFluor 450 (Thermo Fisher Scientific), CD45-FITC (BioLegend), TCRβ-BV421 (BD Biosciences), CD4-PE (BD Biosciences) and CD8-APC-Cy7 (BioLegend). Immune infiltrated cells isolated from the lymphoedematous tissues were characterized by FACS (BD FACSAria III).

Lymphangiography. Lymph, iliac lymph nodes and plasma were collected from mice intradermally injected with Evans Blue (200 µl, 0.5% in PBS; Sigma-Aldrich) at the tip of the tail. The samples were incubated at 55 °C with formamide (Sigma-Aldrich) for 24 h, followed by absorbance measurements with a microplate spectrophotometer (BioTek).

β-Hydroxybutyrate measurements. Mouse plasma and lymph, collected from the vena cava and the thoracic duct, respectively, were mixed with 50:30:20 (methanol:acetonitrile:10 mM Tris, pH 9.3) extraction buffer (1:10). Extracts were then centrifuged for 5 min at 20,000*g*, the supernatant was transferred to LC-MS vials and β-OHB levels were analysed using LC-MS. Isobaric metabolites could not be excluded in our measurements.

Uncorrected Proof

Statistical analysis. Data are represented as mean ± s.e.m. Statistical significance between two groups was determined using the two-tailed, Student's *t*-test or two-tailed, one-sample, Student's *t*-test (Prism v.7.0b), unless otherwise specified. Statistical significance between multiple groups was determined by analysis of variance, followed by individual comparisons performed by Bonferroni's post hoc test (Prism v.7.0b). $P < 0.05$ was considered to be statistically significant.

Reporting Summary. Further information on research design is available in the Nature Research Reporting Summary linked to this article.

Data availability

All data generated or analysed during this study are included in this published article (and its Supplementary Information). The raw data that support the findings of this study are available from the corresponding author on reasonable request. Supplementary Figs. 1, 5 and 6 have associated raw data (uncropped blots) in Supplementary Fig. 7. Figure 3 and Supplementary Fig. 4 have associated raw data (Excel files) with metabolite abundances.

Received: 9 August 2018; Accepted: 11 June 2019;

References

1. Alitalo, K. The lymphatic vasculature in disease. *Nat. Med.* **17**, 1371–1380 (2011).
2. Puchalska, P. & Crawford, P. A. Multi-dimensional roles of ketone bodies in fuel metabolism, signaling, and therapeutics. *Cell Metab.* **25**, 262–284 (2017).
3. Dayan, J. H., Ly, C. L., Kataru, R. P. & Mehrara, B. J. Lymphedema: pathogenesis and novel therapies. *Annu. Rev. Med.* **69**, 263–276 (2017).
4. Avraham, T. et al. Th2 differentiation is necessary for soft tissue fibrosis and lymphatic dysfunction resulting from lymphedema. *FASEB J.* **27**, 1114–1126 (2013).
5. Tabibiazar, R. et al. Inflammatory manifestations of experimental lymphatic insufficiency. *PLoS Med.* **3**, e254 (2006).
6. Cormier, J. N. et al. Lymphedema beyond breast cancer: a systematic review and meta-analysis of cancer-related secondary lymphedema. *Cancer* **116**, 5138–5149 (2010).
7. Rockson, S. G. & Rivera, K. K. Estimating the population burden of lymphedema. *Ann. N.Y. Acad. Sci.* **1131**, 147–154 (2008).
8. Wong, B. W. et al. The role of fatty acid beta-oxidation in lymphangiogenesis. *Nature* **542**, 49–54 (2017).
9. Yu, P. et al. FGF-dependent metabolic control of vascular development. *Nature* **545**, 224–228 (2017).
10. Cotter, D. G., d'Avignon, D. A., Wentz, A. E., Weber, M. L. & Crawford, P. A. Obligate role for ketone body oxidation in neonatal metabolic homeostasis. *J. Biol. Chem.* **286**, 6902–6910 (2011).
11. Bazigou, E. et al. Genes regulating lymphangiogenesis control venous valve formation and maintenance in mice. *J. Clin. Invest.* **121**, 2984–2992 (2011).
12. Detry, B. et al. Sunitinib inhibits inflammatory corneal lymphangiogenesis. *Invest. Ophthalmol. Vis. Sci.* **54**, 3082–3093 (2013).
13. Schoors, S. et al. Fatty acid carbon is essential for dNTP synthesis in endothelial cells. *Nature* **520**, 192–197 (2015).
14. Pinto, A., Bonucci, A., Maggi, E., Corsi, M. & Businaro, R. Anti-oxidant and anti-inflammatory activity of ketogenic diet: new perspectives for neuroprotection in Alzheimer's disease. *Antioxidants* 7(5), 63 (2018).
15. Yamanashi, T. et al. Beta-hydroxybutyrate, an endogenic NLRP3 inflammasome inhibitor, attenuates stress-induced behavioral and inflammatory responses. *Sci. Rep.* **7**, 7677 (2017).
16. Goldberg, E. L. et al. β-Hydroxybutyrate deactivates neutrophil NLRP3 inflammasome to relieve gout flares. *Cell Rep.* **18**, 2077–2087 (2017).
17. Henry, R. A., Kuo, Y. M. & Andrews, A. J. Differences in specificity and selectivity between CBP and p300 acetylation of histone H3 and H3/H4. *Biochemistry* **52**, 5746–5759 (2013).
18. Xu, Y. M., Du, J. Y. & Lau, A. T. Posttranslational modifications of human histone H3: an update. *Proteomics* **14**, 2047–2060 (2014).
19. Peters, A. H. et al. Partitioning and plasticity of repressive histone methylation states in mammalian chromatin. *Mol. Cell* **12**, 1577–1589 (2003).
20. Zhang, X., Wen, H. & Shi, X. Lysine methylation: beyond histones. *Acta Biochim. Biophys. Sin.* **44**, 14–27 (2012).
21. Carey, B. W., Finley, L. W., Cross, J. R., Allis, C. D. & Thompson, C. B. Intracellular alpha-ketoglutarate maintains the pluripotency of embryonic stem cells. *Nature* **518**, 413–416 (2015).
22. TeSlaa, T. et al. α-Ketoglutarate accelerates the initial differentiation of primed human pluripotent stem cells. *Cell Metab.* **24**, 485–493 (2016).
23. Tian, W. et al. Leukotriene B4 antagonism ameliorates experimental lymphedema. *Sci. Transl. Med.* **9** (389), eaal3920 https://doi.org/10.1126/scitranslmed.aal3920 (2017).
24. Zampell, J. C. et al. CD4$^+$ cells regulate fibrosis and lymphangiogenesis in response to lymphatic fluid stasis. *PLoS ONE* **7**, e49940 (2012).
25. Gousopoulos, E., Proulx, S. T., Scholl, J., Uecker, M. & Detmar, M. Prominent lymphatic vessel hyperplasia with progressive dysfunction and distinct immune cell infiltration in lymphedema. *Am. J. Pathol.* **186**, 2193–2203 (2016).
26. Keith, L., Rowsemitt, C. & Richards, L. G. Lifestyle modification group for lymphedema and obesity results in significant health outcomes. *Am. J. Lifestyle Med.* **0**, 1559827617742108 (2017).
27. Hu, X., Jiang, Z. & Liu, N. A novel approach for harvesting lymphatic endothelial cells from human foreskin dermis. *Lymphat. Res. Biol.* **4**, 191–198 (2006).
28. Vandekeere, S. et al. Serine synthesis via PHGDH Is essential for heme production in endothelial cells. *Cell Metab.* **28**, P573–P587 (2018).
29. Muzumdar, M. D., Tasic, B., Miyamichi, K., Li, L. & Luo, L. A global double-fluorescent Cre reporter mouse. *Genesis* **45**, 593–605 (2007).
30. Kalucka, J. et al. Quiescent endothelial cells upregulate fatty acid beta-oxidation for vasculoprotection via redox homeostasis. *Cell Metab.* **28**, P881–P894 (2018).

Acknowledgements

We thank P. Crawford and T. Mäkinen for providing *Oxct1*$^{lox/lox}$ and *Prox1-cre*^{ERT2} mice, respectively. We thank G. Bogaert for providing human foreskins. We also thank S.M. Fendt for discussion and advice. This work was supported by fellowships from LE&RN/FDRS (A.Z.), and supporting grants from IUAP P7/03 (P.C.), Methusalem funding by the Flemish government (P.C.), FWO (G.0598.12, G.0532.10, G.0817.11, G.0834.13, to P.C.), Leducq Transatlantic Network Artemis (P.C.), AXA Research Fund (no. 1465, to P.C.), Foundation against Cancer (P.C.), Fund for Translation Biomedical Research (to P.C.), ERC Advanced Research Grant (EU-ERC269073, to P.C.). We thank A. Van Nuffelen, A. Carton, A. Manderveld, K. Brepoels, K. Peeters, N. Dai, M. Rifaad, M. Parys, I. Betz, C. De Legher, S. Wyns, P.J. Coolen, M. Nijs, P. Vanwesemael, B. Verherstraeten, G. Dubois, E. Van Dyck, A. Acosta Sanchez and D. Verdegem for their technical assistance, and various laboratory members for their feedback and discussions.

Author contributions

M.G.C., A.Z., J.S., A.-C.K.T., L.-A.T., W.V., A.B., R.M.P., S.V., I.C. and B.G. performed research and/or analysed the data. P.d.Z. managed the collaboration with UZ Leuven, wrote the documentation for the Medical Ethical Committee agreement and the informed consent for HDLEC subjects. M.G.C., A.Z., R.M.P., M.M., G.E., M.D. and P.C. designed experiments. M.G.C., A.Z. and P.C. wrote the paper. P.C. conceptualized and supervised the study. All authors discussed the results and commented on the manuscript.

Competing interests

The authors declare no competing financial or non-financial interests in relation to the work described.

Additional information

Supplementary information is available for this paper at https://doi.org/10.1038/s42255-019-0087-y.

Reprints and permissions information is available at www.nature.com/reprints.

Correspondence and requests for materials should be addressed to P.C.

All applicable international, national and/or institutional guidelines for the care and use of human samples were followed. All applicable international, national and/or institutional guidelines for the care and use of animals were followed. All procedures performed in experiments involving animals were in accordance with the ethical standards of the institution and with the approval of the institutional ethical committee for animal experimentation.

Peer review information: Primary Handling Editor: P. Jha

Publisher's note: Springer Nature remains neutral with regard to jurisdictional claims in published maps and institutional affiliations.

© The Author(s), under exclusive licence to Springer Nature Limited 2019

Uncorrected Proofs

nature research

Corresponding author(s): Peter CARMELIET

Reporting Summary

Nature Research wishes to improve the reproducibility of the work that we publish. This form provides structure for consistency and transparency in reporting. For further information on Nature Research policies, see Authors & Referees and the Editorial Policy Checklist.

Statistical parameters

When statistical analyses are reported, confirm that the following items are present in the relevant location (e.g. figure legend, table legend, main text, or Methods section).

n/a	Confirmed	
☐	☒	The exact sample size (*n*) for each experimental group/condition, given as a discrete number and unit of measurement
☐	☒	An indication of whether measurements were taken from distinct samples or whether the same sample was measured repeatedly
☐	☒	The statistical test(s) used AND whether they are one- or two-sided *Only common tests should be described solely by name; describe more complex techniques in the Methods section.*
☒	☐	A description of all covariates tested
☒	☐	A description of any assumptions or corrections, such as tests of normality and adjustment for multiple comparisons
☐	☒	A full description of the statistics including central tendency (e.g. means) or other basic estimates (e.g. regression coefficient) AND variation (e.g. standard deviation) or associated estimates of uncertainty (e.g. confidence intervals)
☐	☒	For null hypothesis testing, the test statistic (e.g. *F*, *t*, *r*) with confidence intervals, effect sizes, degrees of freedom and *P* value noted *Give P values as exact values whenever suitable.*
☒	☐	For Bayesian analysis, information on the choice of priors and Markov chain Monte Carlo settings
☒	☐	For hierarchical and complex designs, identification of the appropriate level for tests and full reporting of outcomes
☒	☐	Estimates of effect sizes (e.g. Cohen's *d*, Pearson's *r*), indicating how they were calculated
☐	☒	Clearly defined error bars *State explicitly what error bars represent (e.g. SD, SE, CI)*

Our web collection on statistics for biologists may be useful.

Software and code

Policy information about availability of computer code

Data collection	QuantaSmart TM V4 PerkinElmer (scintillation counting), ZEN 2011 software (confocal imaging), Image Quant LAS 4000 V 1.2 (Western-Blot Imager), XF Reader 1.8.1.1 (Seahorse flux analyzer), Gen5 1.11.5 (microtiter plate colorimetric assays), GraphPad Prism Prism version 7.0b (statistical analysis).
Data analysis	GraphPad Prism v7.0b was used for statistical analysis. ImageJ/FIJI 1.50i was used for image analyses. Leica MM AF 2.1 software for morphometric analysis. Flowjo 10.2 software was used for flow cytometric analysis. XCalibur 4.0 (Thermo Scientific) was used for metabolite quantification (LC-MS).

For manuscripts utilizing custom algorithms or software that are central to the research but not yet described in published literature, software must be made available to editors/reviewers upon request. We strongly encourage code deposition in a community repository (e.g. GitHub). See the Nature Research guidelines for submitting code & software for further information.

Data

Policy information about availability of data

All manuscripts must include a data availability statement. This statement should provide the following information, where applicable:

- Accession codes, unique identifiers, or web links for publicly available datasets
- A list of figures that have associated raw data
- A description of any restrictions on data availability

All data generated or analysed during this study are included in this published article (and its supplementary information files). The raw data that support the findings of this study are available from the corresponding author upon reasonable request. Supplementary Figures 1, 5 and 6 have associated raw data (uncropped blots) in Supplementary Figure 7. Figure 3 and Supplementary Figure 4 have associated raw data (Excel files) with metabolite abundances.

Field-specific reporting

Please select the best fit for your research. If you are not sure, read the appropriate sections before making your selection.

☒ Life sciences ☐ Behavioural & social sciences ☐ Ecological, evolutionary & environmental sciences

For a reference copy of the document with all sections, see nature.com/authors/policies/ReportingSummary-flat.pdf

Life sciences study design

All studies must disclose on these points even when the disclosure is negative.

Sample size	For in vitro tests, at least 3 independent biological replicates were performed; for in vivo experiments, at least 3 mice were evaluated for each group (the exact sample size is indicated in the figure legends). No statistical methods were used to predetermine sample size, the sample size was based on previous experience in the lab for each experiment to yield high power to detect specific effects.
Data exclusions	Mice subjected to the tail lymphedema model that developed tail ulcers or tail necrosis were excluded from the analysis. Ulceric/necrotic tails were not included in the study as they could bias the obtained results. This was a pre-established exclusion criterion.
Replication	All data were obtained from independently-repeated experiments with independent biological samples as stated in the figure legends, yielding similar results. All data reported in the manuscript are from biological replicates.
Randomization	Mice were randomly allocated into different groups.
Blinding	The investigators performing data analysis were blinded to group/treatment allocation. For experiments involving microscopic analysis of individual (immuno-)stained cells, initial confocal image acquisition was done by researchers blinded to the experimental condition to avoid biased imaging of cells presenting a certain phenotype.

Reporting for specific materials, systems and methods

Materials & experimental systems

n/a	Involved in the study
☒	☐ Unique biological materials
☐	☒ Antibodies
☐	☒ Eukaryotic cell lines
☒	☐ Palaeontology
☐	☒ Animals and other organisms
☐	☒ Human research participants

Methods

n/a	Involved in the study
☒	☐ ChIP-seq
☐	☒ Flow cytometry
☒	☐ MRI-based neuroimaging

Antibodies

Antibodies used	As detailed in the Methods section, these are the primary antibodies that were used in this study, with the supplier name, catalog number, clone name (when available), lot number (when available) and dilution used: - Rabbit polyclonal anti-OXCT1 (Proteintech, 12175-1-AP, lot. 00040183, 1:1000 for immunoblot)

- Rabbit polyclonal anti-alpha-tubulin (Cell Signaling, 2144, 1:1000 for immunoblot)
- Rabbit anti-LYVE1 (Angiobio, 11-034, 1:100 for immunofluorescence)
- Rat anti-CD31 (BD Biosciences, 557355, clone MEC13.3, lot. 8004572, 1:200 for immunofluorescence)
- Rabbit anti-cleaved caspase-3 (Cell Signaling, 9664S, lot. 2, 1:200 for immunofluorescence)
- Anti-actin (Alexa fluor 488 phalloidin) (Thermo Fisher Scientific, A12379, 1:100 for immunofluorescence)
- Anti-annexin V APC-coupled antibody (Thermo Fisher Scientific, A35110, 1:20 for immunostaining)
- Rabbit anti-acetyl lysine (PTM-BioLab, A35110 PTM-105, 1:1000 for immunoblot)
- Rabbit anti-GAPDH (Cell Signaling, 2118, lot. 10, 1:1000 for immunoblot)
- Anti-acetyl-histone and total histone antibodies (Acetyl-Histone Antibody Sampler Kit Cell Signaling Technology, Cell Signaling, 9933T)
- Rabbit anti-histone anti-H3k9ac (Cell Signaling, 9649, lot. 11, 1:1000 for immunoblot, 1:200 for immunofluorescence)
- Rabbit anti-histone H4k8ac (Cell Signaling, 2594, lot. 10, 1:1000 for immunoblot)
- Rabbit anti-histone H3k27me3 (Cell Signaling, C36811, lot. 8, 1:1000 for immunoblot)
- Rabbit anti-histone H2 (Cell Signaling, 2578, lot. 1, 1:1000 for immunoblot)
- Rabbit anti-histone H3 (Cell Signaling, 9715, lot. 9, 1:1000 for immunoblot)
- Rabbit anti-histone H4 (Cell Signaling, 2592, lot. 6, 1:1000 for immunoblot)
- Rabbit anti-VEGFR-3 (Santa Cruz Biotechnology, SC-321, lot. F1714, 1:1000 for immunoblot)
- Rat anti-BrdU (Serotec, OBT0030, 1:100 for immunofluorescence)
- Rabbit anti-Tie2 (Santa Cruz Biotechnology, SC-324, lot. J1909, 1:1000 for immunoblot)
- Rabbit anti-Ang1 (Thermo Fisher Scientific, PA5-78774, 1:1000 for immunoblot)
- Goat anti-VEGFR-3 (R&D Systems, AF743, lot. DAB0217031, 1:50 for immunofluorescence)
- Anti-mouse CD45-PeCy7 (eBioscience, 25-0451-82, clone 30-F11, lot. E07567-1635, 1:700 for flow cytometry)
- Anti-mouse podoplanin-APC (Biolegend, 127410, clone 8.1.1, lot. B217186, 1:100 for flow cytometry)
- Anti-mouse CD31-FITC (Thermo Fisher Scientific, 11-0311-82, clone 390, lot. 1934014, 1:50 for flow cytometry)
- Anti-mouse CD45-FITC (BioLegend, 103107, clone 30-F11, 1:200 for flow cytometry)
- Anti-mouse TCRbeta-BV421 (BD Biosciences, 562839, clone H57-597, lot. 8130587, 1:300 for flow cytometry)
- Anti-mouse CD4-PE (BD Biosciences, 561837, clone RM4-5, lot. 6105713, 1:400 for flow cytometry)
- Anti-mouse CD8-APC-Cy7 (BioLegend, 100713, clone 53-6.7, lot. B260276, 1:400 for flow cytometry)

Validation

Concerning antibody specificity, we kindly refer to the suppliers' websites and datasheets to find statements on specificity and citations for the use of the antibodies.

Eukaryotic cell lines

Policy information about cell lines

Cell line source(s)

Primary human dermal lymphatic endothelial cells (HDLECs), isolated from foreskins (with approval from the Medical Ethical Committee KU Leuven/UZ Leuven and informed consent from all subjects).

Authentication

No cell lines were used, only primary cells were used.

Mycoplasma contamination

Cells were negative for mycoplasma contamination.

Commonly misidentified lines
(See ICLAC register)

No commonly misidentified cell lines were used.

Animals and other organisms

Policy information about studies involving animals; ARRIVE guidelines recommended for reporting animal research

Laboratory animals

C57BL/6J and Prox1-CreERT2;Oxct1lox/lox mice (C57BL/6N), females, 8-12 weeks-old.

Wild animals

This study did not involve wild animals.

Field-collected samples

This study did not involve field-collected samples.

Human research participants

Policy information about studies involving human research participants

Population characteristics

Only healthy males, between 0-10 years old were subjected to circumcision. Subjects did not have any diagnosed disease and were not subjected to any treatment. Foreskin biopsies were obtained with approval from the Medical Ethical Committee KU Leuven/UZ Leuven (protocol S57123) and informed consent from all subjects by their parents.

Recruitment

Subjects were recruited by the criteria mentioned above. Exclusion criteria and potential self-selection were not applied.

Flow Cytometry

Plots

Confirm that:

☐ The axis labels state the marker and fluorochrome used (e.g. CD4-FITC).

☐ The axis scales are clearly visible. Include numbers along axes only for bottom left plot of group (a 'group' is an analysis of identical markers).

☐ All plots are contour plots with outliers or pseudocolor plots.

☐ A numerical value for number of cells or percentage (with statistics) is provided.

Methodology

Sample preparation	See Methods section (pages 20-22).
Instrument	BD FACSAria III (BD Biosciences).
Software	Flowjo 10.2.
Cell population abundance	Not applicable.
Gating strategy	See Methods section (page 23).

☐ Tick this box to confirm that a figure exemplifying the gating strategy is provided in the Supplementary Information.